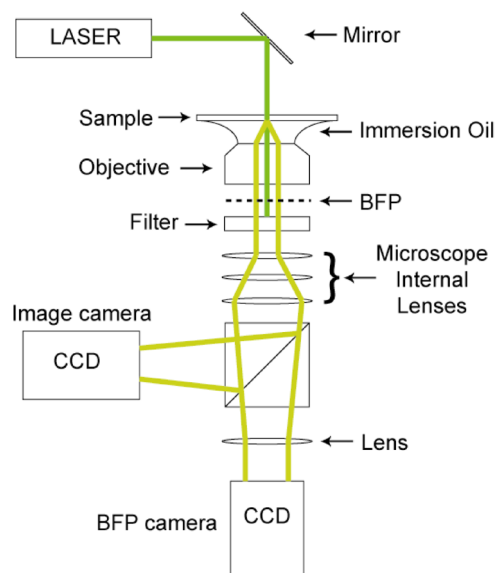# Image Formation in Wide-Field Microscopes Based on Leakage of Surface Plasmon-Coupled Fluorescence

**Volume 1, Number 2, August 2009**

**S. P. Frisbie**

**C. F. Chesnutt**

**M. E. Holtz**

**A. Krishnan**

**L. Grave de Peralta**

**A. A. Bernussi**

# Image Formation in Wide-Field Microscopes Based on Leakage of Surface Plasmon-Coupled Fluorescence

**S. P. Frisbie,**[1] **C. F. Chesnutt,**[2] **M. E. Holtz,**[1] **A. Krishnan,**[1]
**L. Grave de Peralta,**[2] **and A. A. Bernussi**[1]

[1]Department of Electrical and Computer Engineering, Texas Tech University, Lubbock, TX 79409 USA
[2]Department of Physics, Texas Tech University, Lubbock, TX 79409 USA

**Abstract:** A proof-of-concept imaging technique that combines the advantages of wide-field surface plasmon, leakage radiation, and total internal reflection fluorescence microscopy methods is presented. High-contrast non-scanning images with subwavelength resolution of patterned and homogeneous samples coated with a fluorescent material were demonstrated. We show that the image formed in the back focal plane of the objective lens can be reconstructed from the image of the sample's surface using an algorithm similar to that used in computerized tomographic imaging. Our experimental results suggest that there is a 1-D Fourier transform relationship between any line amplitude profile at a given angle passing through the center of the sample's surface image and a line amplitude profile passing through the center of the back-focal-plane image at the same angle.

**Index Terms:** Engineered photonic nanostructures, photonic materials and engineered photonic structures, optics, fluorescence microscopy, microscopy, imaging, plasmonics, nanophotonics.

## 1. Introduction

Surface plasmon resonance (SPR) microscopy using prism coupling in the Kretschmann configuration was proposed several years ago as an alternative technique to obtain ultra-high-resolution images owing to the resonant mechanism of contrast formation [1]–[3]. However, this approach may produce distorted images, has restricted numerical aperture (NA), which limits the maximum angle for light collection, and has limited magnification. Other microscopy techniques based on SPR excitation have been reported with the aim of further improvements in image contrast and sensitivity [4], [5]. Recent progress in SPR microscopy concerns the substitution of the prism configuration [6] by a high-NA oil-immersion objective lens to couple light into and/or from the SPR coupled modes [7]–[9]. Wide-field surface plasmon (WFSP) [7], [10] and leakage radiation (LR) [8], [11], [12] are examples of newly developed SPR microscopy techniques that rely on the collection of the surface plasmon-coupled radiation with a high-NA microscope objective lens. This approach is similar to the widely used through-the-objective configuration in total internal reflection fluorescence (TIRF) microscopy [13], which solves the image distortion problem, has a high NA for light collection, and provides high image magnification. In both WFSP and LR microscopy, the sample to be imaged is in direct contact with a thin metal film, which is usually silver or gold, with a thickness of several tens of

nanometers deposited on a glass substrate. Small variations in thickness or refractive index in the sample result in abrupt changes in the phase and intensity of the light collected by the high-NA objective lens under SPR conditions [4], [9]. This translates into high image contrast between areas of the sample that slightly differ in thickness or refractive index. In WFSP microscopes, an oil-immersion objective lens in direct optical contact with the glass side of the glass-metal-sample arrangement is used for both sample illumination and collection of the light reflected from the sample [7], [10]. In this approach, a spatial light modulator is used to illuminate the sample at a narrow range of incidence angles necessary for exciting the SPR in the glass-metal-sample arrangement [7], [10]. In addition, a rotating diffuser is used to remove undesirable speckle noise on the image when a laser is used as the illumination source [7]. In contrast to the WFSP approach, LR microscopy dispenses with the need for spatial light modulators and rotating diffusers and uses only the high-NA objective lens to collect the plasmon-coupled LR [8], [11], [12]. However, in the LR approach a second low-NA objective lens is required to excite the SPR in the sample under investigation. LR microscopes have been primarily used to image the propagation of surface plasmons [8], [11], [12] while WFSP microscopes have been used to obtain 2-D non-scanning (wide-field) images with subwavelength lateral resolution [7], [10]. Although high-contrast and high-resolution images have been obtained with WFSP and LR, these techniques require relatively complex optical instrumentation, and the image resolution depends on the polarization of the input light source.

In this paper, we present for the first time a new imaging technique that combines advantages of WFSP, LR, and TIRF microscopy techniques. We show that high-contrast images with subwavelength resolution from patterned and unpatterned samples can be obtained with this technique, regardless of the polarization of the excitation laser source. In our approach, the glass-metal-sample arrangement is modified by adding a top thin layer comprised of a dye-doped dielectric material. The LR, due to plasmon-coupled fluorescence, is then collected by a high-NA oil-immersion objective lens. Similar to the WFSP technique, our approach, denoted wide-field leakage plasmon-coupled fluorescence (WFLPCF) microscopy, permits us to obtain non-scanning images of the sample surface and dispenses with the need for spatial light modulators and diffusers, greatly simplifying its practical implementation. Similar to WFSP and LR microscopes, our approach permits simultaneous imaging of the sample surface and its corresponding Fourier transform plane. However, the use of plasmon-coupled fluorescence for imaging in a LR configuration allows us to perform a detailed quantitative study of the image formation in this type of microscope. Our results indicate that the image formed at the back focal plane (BFP) of the high-NA objective lens is not related to the surface of the sample through a simple two-dimensional Fourier transform (2-D-FT). We demonstrate that images formed at the BFP can be reconstructed using an algorithm based on the superposition of one-dimensional Fourier transform (1-D-FT) line profiles at different angles of the image of the sample's surface.

## 2. Experimental Setup and Sample Preparation

A schematic illustration of the WFLPCF microscope is shown in Fig. 1. In our arrangement, a Nikon Eclipse TE-300 inverted microscope was modified to implement the proposed technique. The samples, coated with a fluorescent material, are illuminated with a diode laser $(\lambda = 532 \text{ nm})$. Leakage of plasmon-coupled fluorescence is collected by a 100X immersion oil objective lens $(\text{NA} = 1.3)$. The collimated BFP emission from the objective is then transmitted through a bandpass or a longpass filter to block the direct beam from the laser. A set of three lenses, internal to the Nikon microscope, perform magnification and aberration correction along with image formation. A CCD camera captures the image of the sample surface after being partially reflected by the beam splitter. An external lens and a second CCD camera collect the image formed in the BFP of the objective. The BFP image corresponds to the Fourier plane with respect to the sample surface emission and thus to a map of the 2-D momentum distribution of the plasmon-coupled fluorescence leaked into the substrate [7], [8], [10]–[12]. Note that our proposed microscope dispenses with the use of spatial light modulators and rotating diffusers, which greatly simplifies its practical realization and reduces the number of optical components in the microscope.
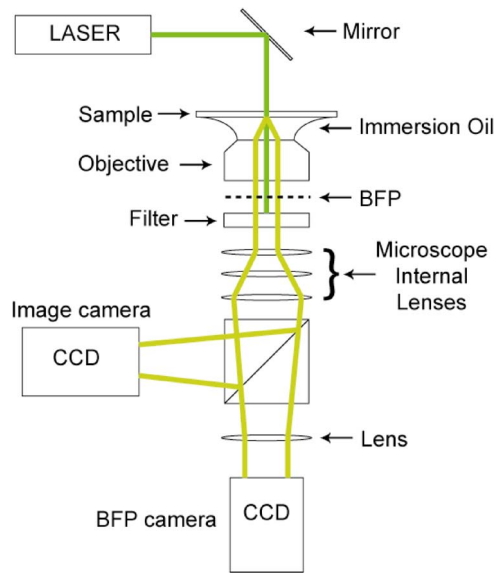
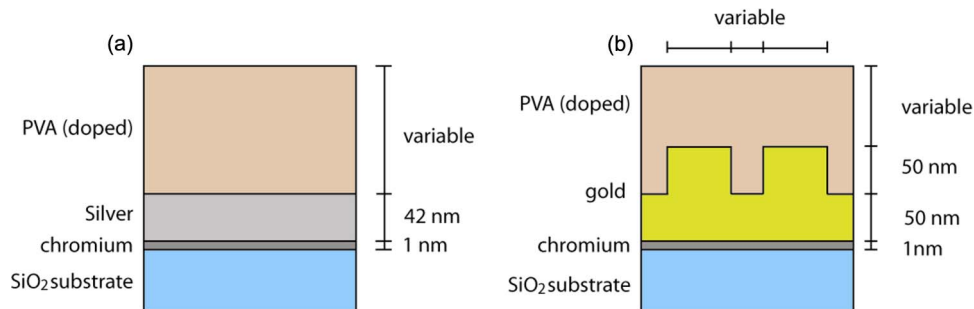Fig. 1. Schematic diagram of the of the WFLPCF microscope.



Fig. 2. Schematic illustration of (a) unpatterned and (b) patterned sample structures.

Imaging with the WFLPCF microscope can be performed using homogeneous and patterned samples. Examples of sample structures investigated in this work are illustrated in Fig. 2. Homogeneous samples [see Fig. 2(a)] are comprised of a glass cover slip substrate, an ~1-nm-thick chromium adhesion layer, followed by a 42-nm-thick silver layer. A layer of 1–10% by weight poly(vinyl) alcohol (PVA) doped with ~1-mM rhodamine 6G (R6G), with emission maximum at wavelength ~566 nm, was spun on the top of the silver layer. The thickness of this layer was adjusted by varying the concentration of the PVA material and typically ranged from 100 to 1000 nm. In order to remove any solvent excess from the PVA layer, a post-baking step (1 min at 160 °C) was performed on all samples. Following all measurements, the PVA-R6G layer is easily removed using alcohol and water rinsing.

The patterned samples [see Fig. 2(b)] consist of a glass substrate, an ~1-nm-thick chromium adhesion layer, a sequence of stripes of gold film with two different thicknesses, and the PVA-R6G layer with similar characteristics to that used in the fabrication of the homogenous samples. A 50-nm-thick gold layer is initially deposited on top of the chromium layer. The gold layer is covered with poly(methyl methacrylate) (PMMA) as the resist for e-beam patterning. A pattern, consisting of 300-$\mu$m-long periodic stripes 2 $\mu$m wide separated by 2 or 6 $\mu$m, was written onto the PMMA layer by e-beam lithography. An additional patterned sample with 200-nm stripe width separated by 610 nm was also fabricated with the objective of exploring the resolution limit of the proposed microscope. After developing the PMMA, a second 50-nm-thick layer of gold was evaporated on the top of the
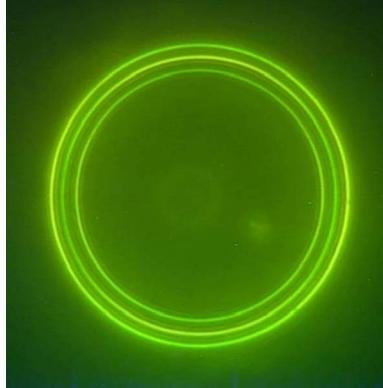
Fig. 3. BFP image from a homogeneous glass/silver/PVA-R6G with an ∼990-nm-thick top layer.

PMMA. A liftoff step produced the patterned stripes and finally the PVA-R6G layer was spun on the top of the patterned structure. When the samples are illuminated by the laser source, the emitted radiation from the fluorescent material couples to the thinner (50 nm) gold region producing sharp and well-defined SPRs. In contrast, in the thicker (100 nm) gold regions the SPR coupling is reduced and the resonances are significantly less pronounced. Differences in the SPR absorption/emission in the patterned gold give rise to high-contrast images.

## 3. Experimental Results and Analysis

### 3.1. Homogeneous Sample

A BFP image of a glass/silver/PVA-R6G homogeneous sample [see Fig. 2(a)], obtained using the WFLPCF microscope, is shown in Fig. 3. Three distinct concentric rings are observed corresponding to three different guided wave polariton modes in the asymmetric metal/dielectric/air waveguide [14], [15]. The weak background light intensity is produced by the fluorescent light which transmits through the thin metal layer without coupling to the SPR. When the PVA- R6G layer is illuminated by the laser source, fluorescent light is emitted in all directions. A fraction of the emitted light is coupled to various guided polariton modes [14], [15]. The leakage plasmon-coupled fluorescence, which is rotationally symmetric [16]–[18], gives rise to a BFP image corresponding to single or multiple concentric bright rings of different radii ($r_{ring}$). The number of rings depends on the thickness of the PVA-R6G layer [14], [15]. All BFP images are formed over a weakly circular background of radius ($r_{cir} > r_{ring}$) corresponding to the maximum collection angle of LR for the high-NA objective lens [9], [11].

The SPR angles ($\theta_{SPR}$) can be determined from the observed rings in the BFP using the following expression:

$$\theta_{SPR} = \operatorname{asin}\left(\frac{r_{ring}}{r_{cir}}\frac{NA}{n}\right) \tag{1}$$

where n = 1.515 is the refractive index of the immersion oil and $asin(NA/n)$ is the maximum angle of the light than can be captured by the objective lens. Using an omnidirectional light source, without any sample, the background radius $r_{cir} = 181$ pixels was determined using the high-NA objective lens as captured by the CCD. Then, using the radius $r_{cir}$ as a reference, we determined radii of curvatures of 142, 156, and 170 pixels for the three rings shown in Fig. 3. Conversion from radii to angles using Eq. (1) yields SPR angles of 42.3°, 47.7°, and 53.7°, respectively. These values were verified by carrying out simulations using the transfer matrix method [1], [14] for the same homogenous sample. In these simulations (not shown), we used a 990-nm-thick dielectric PV-R6G layer with refractive index $n_{diel} = 1.515$ matched to the substrate. The top dielectric layer thickness
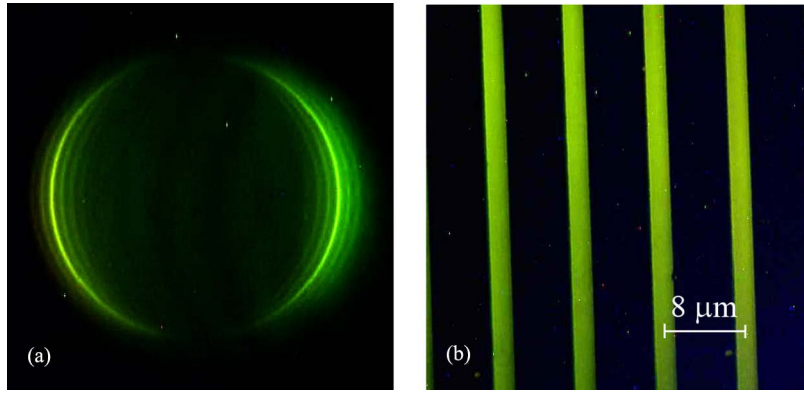
Fig. 4. (a) Polarized BFP image and (b) top surface image of a patterned sample comprising periodic lines. Dark regions correspond to a 6-$\mu$m-wide, 100-nm-thick gold layer and bright regions to a 2-$\mu$m-wide, 50-nm-thick gold layer.

was verified by profilometer measurements. The relatively thick top dielectric layer supports seven surface waveguide plasmon related resonances. This was also verified experimentally by performing angular-emission measurements in the same sample using a hemicylindrical prism configuration [16]. Excellent agreement between simulated and determined SPR angles was obtained for the first three SPR angles corresponding to the rings shown in Fig. 3. The remaining four angular resonances occur at angles that are above the maximum acceptance angle ($\sim$59°) of the immersion objective and could not be collected by the lens.

Using Eq. (1), the real part of the wave-vector $k_{\|\text{ring}} = k_0\, n \sin(\theta_{\text{SPR}})$ corresponding to each SPR can be determined directly from the BFP image shown in Fig. 3 using the expression

$$k_{\|ring} = k_0 \left( \frac{r_{ring}}{r_{cir}} \right) NA \tag{2}$$

where $k_o$ is the real part of the wave-vector in a vacuum of the fluorescence radiation, and $n$ is the refractive index of the dielectric doped layer. Eq. (2) shows that the $k_{\|\text{ring}}$ corresponding to the plasmon guided modes can be determined directly from the radii of curvatures of the SPR rings in the BFP image, without any prior knowledge of the emission angles. Consequently, the wave-vector difference $\Delta k_\|$, corresponding to two arbitrary rings related to different SPR rings in the BFP image, is proportional to the difference between their radii $\Delta r$ through the following relation:

$$\Delta k_\| = k_0 \left( \frac{\Delta r}{r_{cir}} \right) NA. \tag{3}$$

In the case of the BFP image from the homogeneous sample shown in Fig. 3, we determined $\Delta k_\| = 2.23\ \mu\text{m}^{-1}$ corresponding to the inner and outer rings.

### 3.2. Patterned Samples

Additional information about the sample structure can also be extracted from the BFP image. Simultaneous BFP and surface images of the glass/Cr/Au/PVA-R6G patterned sample with a period of 8 $\mu$m [see Fig. 2(b)] obtained by the WFLPCF microscope are shown in Fig. 4(a) and (b), respectively. In this case, the thickness of the PVA-R6G layer spun on the top of the patterned sample was $\sim$255 nm. The images shown in Fig. 4 were obtained by positioning a linear polarizer in the optical path before the filter (see Fig. 1) with transmission axis oriented perpendicular to the stripes of the sample. This blocks the top and bottom portions of the emitted rings in the BFP [see Fig. 4(a)], corresponding to the emission perpendicular to the polarizer state. This results in a better definition of the fringes in Fig. 4(a) but does not alter the quality of the sample's image. The image of the patterned sample [see Fig. 4(b)] exhibits a high contrast with clear edge definition. An estimate
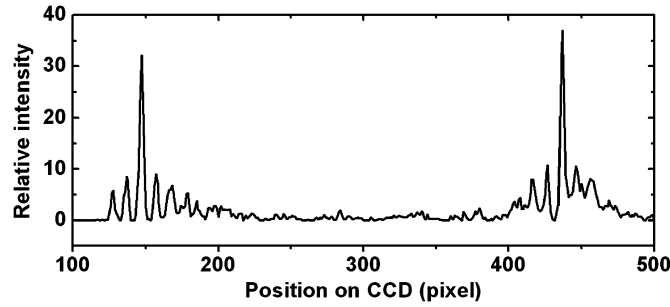
Fig. 5. Intensity line profile at the center of the BFP image shown in Fig. 4(a), after subtraction of the background intensity.

of the image contrast between bright ($I_{bright}$) and dark ($I_{dark}$) intensity regions shown in Fig. 4(b), which can be calculated as $(I_{bright} - I_{dark})/(I_{bright} + I_{dark})$, provides an average contrast of $\sim$0.95. The reduced thickness of the doped dielectric layer allows observation of only one ring in the BFP, thus simplifying the information extraction. The BFP image [see Fig. 4(a)] shows clear periodic modulation in the vicinity of the original emission ring due to the periodic line structure of the sample.

In order to obtain quantitative information about the periodic structure observed in the BFP we performed a horizontal line intensity profile at the center of the image displayed in Fig. 4(a). Fig. 5 shows the centerline profile of the BFP image after subtraction of the image background fluorescence. The intensity profile clearly shows two high-intensity peaks corresponding to the single SPR emission of the structure and a series of periodic satellite peaks symmetrically located on both sides of the main emission peaks. We determined from Fig. 5 an average peak separation of 10 pixels.

Using the wave-vector difference between rings with different radii in the BFP image and described by Eq. (3), the period of the stripes ($\Lambda$) in the patterned sample can be determined from the period of the modulations ($\Delta r_m$) obtained from the line intensity profile shown in Fig. 5 using the expression

$$\Delta k_{\parallel} = \frac{2\pi}{\Lambda} = k_0 \left( \frac{\Delta r_m}{r_{cir}} \right) NA. \tag{4}$$

From Eq. (4), we determined a period of $\sim$7.9 $\mu$m, which in is good agreement with the period of the patterned sample.

In order to illustrate the performance of the proposed microscope, we show in Fig. 6 WFLPCF and SEM top-view images of the patterned sample with 200-nm stripe width separated by 610 nm. A good correspondence between the SEM and the WFLPCF images is evident. The WFLPCF image shows well-defined features corresponding to the fabricated stripes patterned in the sample. The transition between dark/bright regions from the image at 10% and 90% of the average intensity of the bright regions was determined as $\sim$150 nm. Fig. 6 clearly demonstrates that images with subwavelength features can be observed with the proposed microscope.

### 3.3. Relationship Between the Sample and BFP Images

Fig. 7 shows non-polarized BFP images of two glass/Cr/Au/PVA-R6G patterned samples [see Fig. 2(b)] with periods 8 $\mu$m [see Fig. 7(a)] and 4 $\mu$m [see Fig. 7(b)]. Similarly to the results shown in Fig. 4(a), the most intense emission ring of radius $r_{ring}$ is the main feature in both BFP images. This corresponds to the emission cone due to the leakage of plasmon-coupled fluorescence of a homogeneous sample [16], [17]. The weak background in Fig. 7 is due to a small fraction of the fluorescent radiation that is transmitted directly through the thin metal layer without plasmon coupling. The BFP images shown in Fig. 7 also exhibit clear periodic modulations in the vicinity of the main ring due to the periodic line structure of the samples. Similar modulations were previously reported using a WFSP microscope [7]. However, in that case, the image is formed by reflection at
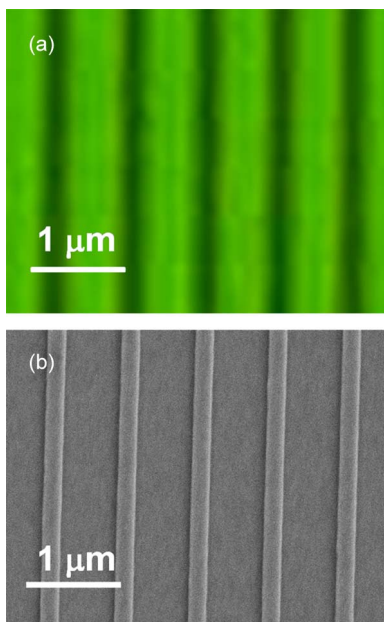
Fig. 6. (a) WFLPCF and (b) SEM top-view images of the patterned sample with 200-nm stripe width separated by 610 nm.
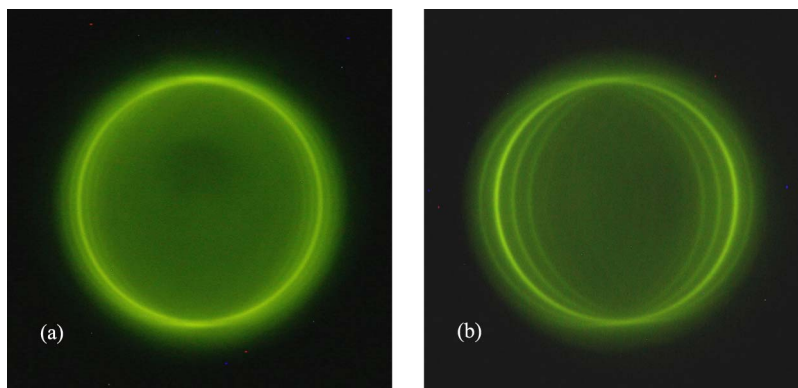


Fig. 7. Unpolarized BFP images of patterned samples comprising lines with (a) 8-$\mu$m and (b) 4-$\mu$m periods.

the sample's surface. Consequently, the modulations appear as poorly defined dark traces over a bright background. This makes a quantitative analysis of the image formation much more difficult. Using the proposed WFLPCF microscope, we are able to perform a comprehensive study of the bright fringes observed in Fig. 7 for the first time. As can be clearly seen in Fig. 7 the separation between consecutive fringes varies with the angle. The maximum separation between fringes occurs in the horizontal direction, which coincides with the transversal direction in the patterned samples. The fringe separation decreases with increasing angle. No modulations are observed in the vertical direction, which coincides with the direction of the stripes in the patterned samples. Fig. 7 also shows that the fringe separation increases as the period of the lines in the patterned samples decreases. Using (4) we determined a period of $\sim$3.9 $\mu$m for $\Delta r_m = 20$ pixels in Fig. 7(b), which is in good agreement with the period of the fabricated sample.

It is clear from Figs. 4 and 7 that the images formed at the BFP do not correspond to a direct 2D-FT of the surface of the patterned sample. In order to reconstruct the BFP images we propose an
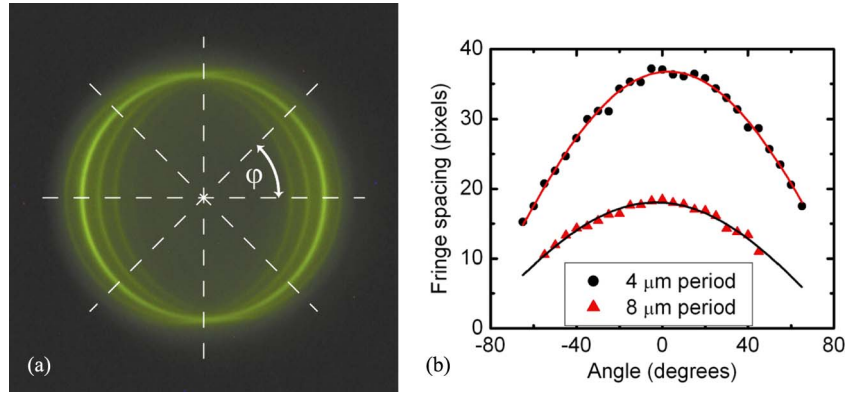
Fig. 8. (a) Line segments at different angles $\varphi$ in the BFP image of the 4-$\mu$m period sample and (b) dependence of the fringe separation $\Delta r$ on the angle $\varphi$ for line intensity profiles obtained from the BFP images shown in Fig. 7(a) [triangles] and Fig. 7(b) [dots]. Solid lines correspond to least square fittings using (5).

algorithm based on the superposition of 1D-FT line profiles of the sample's image at different angles. The dependence of the fringes separation $\Delta r$ on the angle $\varphi$, can be described by the function

$$\Delta r(\varphi) = \cos(\varphi)/\Delta r_m. \tag{5}$$

Expression (5) predicts that the maximum fringe separation in the BFP image of the patterned samples should occur at $\varphi = 0$, and no fringes should be observed at $\varphi = \pi/2$. This is confirmed experimentally from the BFP images shown in Fig. 7. Fig. 8(a) illustrates the line segments used to obtain the intensity profiles at angles $\varphi = 0, \pm\pi/4, \pi/2$ from the BFP image of the patterned sample with 4 $\mu$m period. Measured and simulated fringe separation for patterned samples with 4 and 8 $\mu$m periods are shown in Fig. 8(b) for line profiles with $\varphi$ angles ranging from $-\pi/3$ to $+\pi/3$. Excellent agreement between experiment and simulated results using (5) was obtained for both samples. It is worth noting that substituting (5) into (4) permits us to obtain the correct period of the patterned sample along a line profile with angle $\varphi$

$$\Lambda(\varphi) = \Lambda/\cos(\varphi). \tag{6}$$

Expressions (4)–(6) suggest the existence of a 1D-FT relationship between any line amplitude profile passing through the center of the sample's surface image with an angle $\varphi$ and a line amplitude profile passing through the center of the BFP image with the same angle. This relationship has been proposed previously in the context of generation of surface plasmons at single subwavelength slits [19]. In order to confirm this hypothesis, we suppose that the amplitude of the LR emitted by the sample's surface along the coordinated ($\rho$) line profile $-\infty \leq \rho \leq \infty$ with angle $\varphi$ can be described by the following expressions [20]:

$$f(\rho, \varphi) = f_+(\rho, \varphi) + f_-(\rho, \varphi) \tag{7}$$

$$f_\pm(\rho, \varphi) = a e^{\pm 2\pi i r_{ring}\rho} \left[ comb\left(\frac{\rho}{p/\cos\varphi}\right) \otimes rect\left(\frac{\rho}{w/\cos\varphi}\right) \right]. \tag{8}$$

Each $f_\pm$ function describes an infinite periodic profile in the $\rho$-coordinate described by the convolution ($\otimes$) between a *comb* and a rectangular (*rect*) function [20]. In (8), $a$ is the amplitude of the LR, $\rho$ is the period of the patterned sample, and $w$ is the width of the stripes. The $\pm$ signs correspond to the LR in opposite directions. The factor $e^{\pm 2\pi i r_{ring}\rho}$ represents the phase associate with the plasmon-coupled fluorescence emission cone [16], [19]. Consequently, the linear intensity profiles in the $r$-coordinate $-\infty \leq r \leq \infty$ with an angle $\varphi$ corresponding to the BFP image can be described by the following expression:

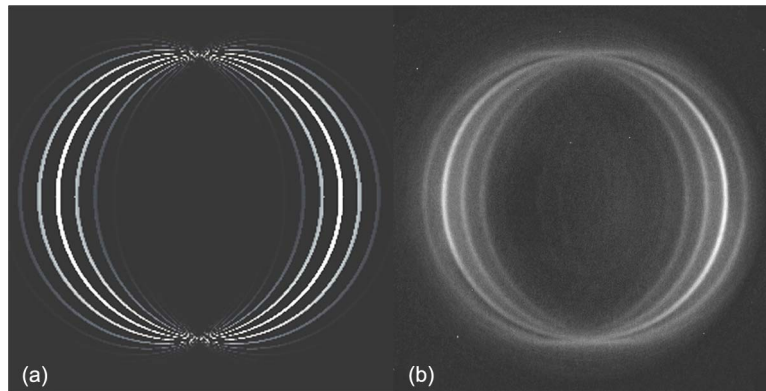$$I(r, \varphi) \propto [g_+(r, \varphi) + g_-(r, \varphi)]^2 \tag{9}$$

Fig. 9. (a) Simulated distribution of local intensity maxima corresponding to a 1-D grating with a period of 4 $\mu$m. (b) BFP image shown in Fig. 7(b).

where the $g_\pm$ functions are 1D-FT of the $f_\pm$ functions. Fig. 9(a) shows simulated intensity maxima using the expression (7)–(9) with $\rho = 8$ $\mu$m and $w = 2$ $\mu$m. For comparison purposes, we show in Fig. 8(b) the BFP image measured for the patterned sample with 4 $\mu$m period. The reconstructed 2-D BFP image [see Fig. 9(a)] was obtained by combining numerous intensity profiles at different angles $\varphi$. An excellent agreement between simulated and measured BFP images is evident. Note that the most external simulated fringe shown in Fig. 9(a) was not observed in the corresponding BFP image shown in Fig. 9(b). This difference is attributed to the limitation in the maximum wave-vector that can be captured by the objective lens.

The 1-D-FT relationship between the surface structure of the sample and the BFP image results shown in Fig. 9 suggests a similarity with the image formation in computerized tomographic techniques [21] rather than the 2D-FT relationship typical of ordinary optical microscopes [20]. This analysis was only made possible due to the high-quality BFP images obtained with our microscope.

## 4. Conclusion

We proposed and demonstrated a new SPR-based microscope that relies on plasmon-coupled fluorescence for sample illumination. Similar to WFSP microscopes, our approach permits acquisition of non-scanning images. In addition, the WFLPCF microscope eliminates the need for spatial light modulators and rotating diffusers, which greatly simplifies its practical realization and reduces the number of optical components of the microscope. Images with subwavelength features can be obtained with our microscope. The proposed technique allows for simultaneous observation of the sample surface and its corresponding image in the reciprocal space. High-contrast images that are independent of the polarization of the laser source are demonstrated with the proposed technique. We have shown that additional information about the sample features, including top-layer thickness and periodicity of the patterned structure, can be determined from the images in the BFP. Our results were validated by complementary measurements of emission versus angle of incidence in the same samples and by simulation analysis of the SPR resonances.

We demonstrate the use of a microscope based on LR for direct wide-field imaging. This permitted us to perform a comprehensive study of the relationship between the sample's and BFP images obtained in our microscope for the first time. We have demonstrated that the BFP image formed by leakage of plasmon-coupled fluorescence from a patterned sample is not the 2-D-FT of the sample's surface structure as in traditional optical microscopes. In addition, we show for the first time that the BFP image can be reconstructed from the structure of the sample's surface following an algorithm that resembles the one used in computerized tomographic imaging. Our experimental results strongly suggest that there is a 1-D-FT relationship between any amplitude line profile along the center of the image of the sample's surface at a given angle and a line amplitude profile along the center of the BFP image with the same angle.

## References

[1] H. Raether, *Surface Plasmons on Smooth and Rough Surfaces and on Gratings*. Berlin, Germany: Springer-Verlag, 1988.

[2] E. Yeatman and E. Ash, "Surface plasmon microscopy," *Electron. Lett.*, vol. 23, no. 20, pp. 1091–1902, Sep. 1987.

[3] B. Rothenhäusler and W. Knoll, "Surface-plasmon microscopy," *Nature*, vol. 332, pp. 615–617, Apr. 1988.

[4] A. N. Grigorenko, A. A. Beloglazov, P. I. Nikitin, C. Kuhne, G. Steiner, and R. Salzer, "Dark-field surface plasmon resonance microscopy," *Opt. Commun.*, vol. 174, no. 1–4, pp. 151–155, Jan. 2000.

[5] A. G. Notcovich, V. Zhuk, and S. G. Lipson, "Surface plasmon resonance phase imaging," *Appl. Phys. Lett.*, vol. 76, no. 13, pp. 1665–1667, Mar. 2000.

[6] E. Kretschman and H. Raether, "Radiative decay of nonradiative surface plasmons excited by light," *H. Z, Naturforsch Part A*, vol. 23, p. 2135, 1968.

[7] G. Stabler, M. G. Somekh, and C. W. See, "High-resolution wide-field surface plasmon microscopy," *J. Microsc.*, vol. 214, no. 3, pp. 328–333, May 2004.

[8] A. Drezet, A. Hohenau, A. L. Stepanov, H. Ditlbacher, B. Steinberger, N. Galler, F. R. Aussenegg, A. Leitner, and J. R. Krenn, "How to erase surface plasmon fringes," *Appl. Phys. Lett.*, vol. 89, no. 9, p. 091117, Aug. 2006.

[9] H. Kano and W. Knoll, "Locally excited surface-plasmon-polaritons for thickness measurement of LBK films," *Opt. Commun.*, vol. 153, no. 4–6, pp. 235–239, Aug. 1998.

[10] M. Mahadi Abdul Jamil, M. C. T. Denyer, M. Youseffi, S. T. Britland, S. Liu, C. W. See, M. G. Somekh, and J. Zhang, "Imaging of the cell surface interface using objective coupled widefield surface plasmon microscopy," *J. Struct. Biol.*, vol. 164, no. 1, pp. 75–80, Oct. 2008.

[11] S. Massenot, J. Grandidier, A. Bouhelier, G. Colas des Francs, L. Markey, J.-C. Weeber, A. Dereux, J. Renger, M. U. Gonzàlez, and R. Quidant, "Polymer-metal waveguides characterization by Fourier plane leakage radiation microscopy," *Appl. Phys. Lett.*, vol. 91, no. 24, p. 243 102, Dec. 2007.

[12] A. Drezet, A. Hohenau, D. Koller, A. Stepanov, H. Ditlbacher, B. Steinberger, F. R. Aussenegg, A. Leitner, and J. R. Krenn, "Leakage radiation microscopy of surface plasmon polaritons," *Mater. Sci. Eng. B*, vol. 149, no. 3, pp. 220–229, Apr. 2008.

[13] D. Axelrod, "Total internal reflection fluorescence microscopy in cell biology," *Traffic*, vol. 2, no. 11, pp. 764–774, Nov. 2001.

[14] S. P. Frisbie, A. Krishnan, X. Xu, L. Grave de Peralta, S. A. Nikishin, M. W. Holtz, and A. A. Bernussi, "Optical reflectivity of asymmetric dielectric-metal-dielectric planar structures," *J. Lightw. Technol.*, vol. 27, no. 15, pp. 2964–2969, Aug. 2009.

[15] I. Gryczinski, J. Malicka, K. Nowaczyk, Z. Gryczynski, and J. Lacowicz, "Effects of sample thickness on the optical properties of surface plasmon-coupled emission," *J. Phys. Chem. B*, vol. 108, no. 32, pp. 12 073–12 083, Jul. 2004.

[16] I. Gryczynski, J. Malicka, Z. Gryczynski, and J. R. Lakowicz, "Surface plasmon-coupled emission with gold films," *J. Phys. Chem. B*, vol. 108, no. 33, pp. 12 568–12 574, Jul. 2004.

[17] S. Smith, Y. Kostov, G. Rao, I. Gryczynski, J. Malicka, Z. Gryczynski, and J. R. Lakowicz, "First observation of surface plasmon-coupled emission due to LED excitation," *J. Fluoresc.*, vol. 15, no. 6, pp. 895–900, Nov. 2005.

[18] I. Gryczynski, J. Malicka, K. Nowaczyk, Z. Gryczynski, and J. R. Lakowicz, "Waveguide-modulated surface plasmon-coupled emission of Nile blue in poly(vinyl alcohol) thin films," *Thin Solid Films*, vol. 510, no. 1/2, pp. 15–20, Jul. 2006.

[19] J.-Y. Laluet, Drezet, C. Genet, and T. W. Ebbesen, "Generation of surface plasmons at single subwavelength slits: From slit to ridge plasmon," *New J. Phys.*, vol. 10, p. 105 014, Oct. 2008.

[20] J. W. Goodman, *Introduction to Fourier Optics*. New York: McGraw-Hill, 1968.

[21] A. C. Kak and M. Slaney, *Principles of Computerized Tomographic Imaging*. New York: IEEE Press, 1988.